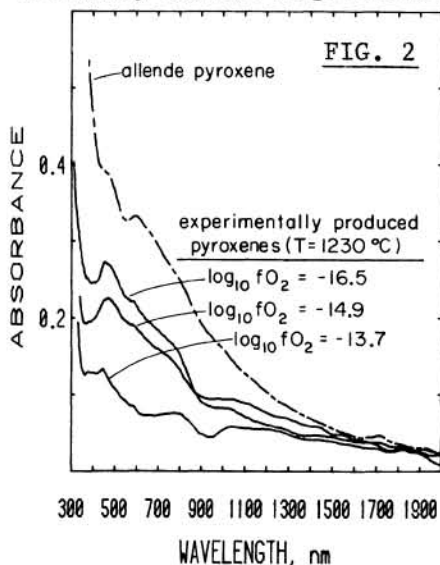


THE INFLUENCE OF OXYGEN FUGACITY AND COOLING RATE ON THE CRYSTALLIZATION OF Ca-Al-RICH INCLUSIONS FROM ALLENDE. E. Stolper, J. Paque, and G.R. Rossman, Div. Geol. Planet. Sci., Caltech, Pasadena, CA 91125

Although there appears to be general agreement that some coarse-grained Ca-Al-rich inclusions (CAIs) from Allende passed through a molten or partially molten stage in their evolution, there are several competing hypotheses to account for the formation of the liquid phase in CAIs (e.g., 1-4). Studies of the phase equilibria of CAI compositions can help distinguish between these mechanisms for generating liquids in CAIs. For example, CAIs formed by condensation of supercooled liquid droplets (4) would be expected to have textures that differ significantly from those of partially molten droplets formed by near-equilibrium condensation (3). Equilibrium condensates would be expected to have crystallized at oxygen fugacities compatible with a nebular gas, whereas inclusions processed in planetary environments or by kinetically-dominated mechanisms need not reflect such an equilibration. We report here preliminary results of experiments that explore the effects of oxygen fugacity and cooling rate on the mineral chemistries, crystallization sequences, and textures of CAIs and show how these can yield insights into CAI evolution.

OXYGEN FUGACITY DURING CAI CRYSTALLIZATION. The presence of Ti^{3+} and Ti^{4+} in pyroxenes in CAIs is well documented (5). Since the Ti^{3+}/Ti^{4+} of pyroxene at a given temperature is expected to be a monotonic function of fO_2 , it is possible to determine the fO_2 levels at which these pyroxenes equilibrated by finding the conditions necessary to duplicate the Ti^{3+}/Ti^{4+} of the natural pyroxenes. A glass similar in composition to a typical Allende fassaite (CaO 23.7, MgO 10.9, Al_2O_3 20.1, SiO_2 40.2, TiO_2 5.1 wt %) was used as a starting material. Oxygen fugacities were controlled by H_2-CO_2 gas mixtures in which samples were suspended for 1-5 days at 1230°C on Pt wire loops. A solid electrolyte sensor, calibrated at the Fe/FeO buffer, was used to measure fO_2 values. One experiment was conducted in air. The experimental results are unreversed. Run products consist primarily of clinopyroxene, with glass, plagioclase, olivine, and spinel. Macroscopically, they vary from white in air, to grey (with a pink-purple tinge) at the Ti_3O_5/TiO_2 buffer, to black (with a blue-purple tinge) near the Ti_2O_3/Ti_3O_5 buffer. In thin section, the reduced pyroxenes show weak pink to green pleochroism.

Experimentally produced pyroxenes were analyzed by electron microprobe and the amount of Ti^{3+} was calculated assuming R_2O_3 stoichiometry. Such recalculations are to be interpreted with caution, both because of their precision (i.e., they are very sensitive to small uncertainties in the analyses) and their accuracy (i.e., the assumption of stoichiometry is questionable [6]). The results of these recalculations are shown in Fig. 1, in which Ti^{3+}/Ti^{4+} is shown versus fO_2 . These results suggest, assuming that Allende pyroxenes crystallized near 1230°C (approximately the temperature at which pyroxene begins to crystallize from a melt of CAI composition), that the fO_2 levels at which they crystallized were lower than the lowest levels achieved in our experiments. Extrapolating the experimentally determined trend to the range of Ti^{3+}/Ti^{4+} ratios of Type B Allende pyroxenes suggests $\log_{10} fO_2$ values of about -17.5 to -22.5. Since almost the full range of Ti^{3+}/Ti^{4+} ratios can be observed in a single inclusion (7), it is unlikely that this range reflects a real variation in fO_2 level at a single temperature.



The oxygen fugacity of the nebular gas ($H_2/H_2O \sim 500-$ to $10^{-18.0}$ atm. Thus, the inferred fO_2 levels for the

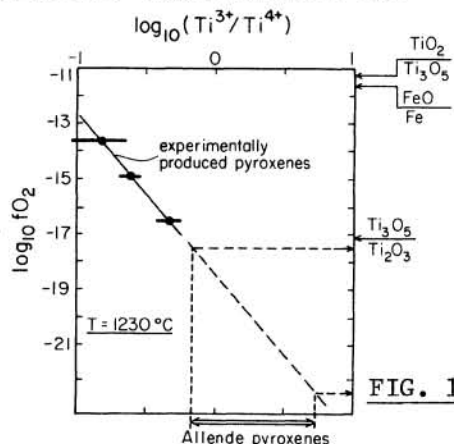


FIG. 1

Optical and near-infrared spectra were taken on experimentally produced pyroxene crystals. The α polarizations of pyroxenes produced at different oxygen fugacities and for a natural Allende pyroxene (NMNH 3529G) are compared in Fig. 2, adjusted to a constant thickness of 50 μm . Aperture sizes ranged from 92-320 μm . All of the pyroxenes figured have 3-6 weight % Ti. The peaks at 470 and 600 nm in natural pyroxene samples with higher Ti contents have been attributed to Ti^{3+} crystal field effects while the broad feature between 700 and 900 nm has been attributed to a $Ti^{3+}-Ti^{4+}$ intervalence charge transfer (8). The growth in the spectra of the experimentally produced pyroxenes of the 470 nm band and the development of a shoulder at 600 nm with decreasing fO_2 and the presence in these spectra of a broad peak from 700-900 nm are not inconsistent with these assignments. These features are on the tail of what is presumably a charge transfer peak in the UV regions of the spectra. The spectra of the experimentally produced pyroxenes begin to approach that of the natural pyroxene at the lowest fO_2 achieved but have not reached it by this point. This corroborates the conclusion based on stoichiometrically determined Ti^{3+}/Ti^{4+} ratios that Allende pyroxenes formed at fO_2 levels lower than the lowest ($10^{-16.5}$ atm, 1230°C) achieved in our experiments.

Crystallization of Ca-Al-rich inclusions

Stolper, E. et. al.

formation of Allende pyroxenes are compatible with equilibration with the gaseous nebula at this temperature. Although not ruling out alternative modes of origin for CAIs, the oxidation state of Allende pyroxenes is compatible with their formation by equilibrium condensation from a cooling nebular gas (e.g., 3, 9).

Crystallization sequences of melts similar in composition to CAIs have been studied in air, and to a first approximation the results appear applicable to actual CAIs (10). However, since CAIs crystallized under reducing conditions at which substantial amounts of Ti^{3+} were present, it is necessary to determine whether crystallization sequences are different at these low fO_2 levels. Synthesis experiments on a composition previously studied in air (10) have been conducted in H_2-CO_2 gas mixtures on Ir wire loops at fO_2 levels approximately 1.2 orders of magnitude more oxidizing than the Ti_2O_3/Ti_3O_5 buffer. Based on Figs. 1 and 2, this is not quite as low as the actual conditions under which CAIs crystallized, but substantial Ti^{3+} is present. Results are compared with synthesis experiments conducted in air in Fig. 3. The temperature of pyroxene entry is raised by about 5°C, but the crystallization sequence (sp + mel + plag + cpx) is the same as in air. These results confirm the validity of phase equilibria determined in air for modelling the crystallization sequences of CAIs.

COOLING RATE STUDIES. The textures and crystallization sequences of those CAIs formed by crystallization of melts depend both on melt composition and the time-temperature history of the inclusion. Until now, only equilibrium crystallization sequences have been studied (e.g., 10). A series of controlled cooling rate experiments has been conducted on a melt similar in composition to an average Type B CAI. Experiments were conducted in air on the same composition used in (10). Samples were held at 25–30°C above the liquidus for 3 hours on Pt wire loops and then cooled at approximately linear cooling rates of 2–200°C/hour. By quenching samples at different temperatures, the crystallization sequence at each cooling rate and the development of textures could be observed. Spinel was the first phase to crystallize and melilite the second over this range of cooling rates. Melts were supercooled by 50°C or more before spinel began to crystallize, while melilite, which appears at 1400°C in the equilibrium crystallization sequence, began to crystallize at 1150–1190°C at all cooling rates studied. Clinopyroxene was the third phase to crystallize at 20–200°C/hour, appearing at ~1125°C. This contrasts with the equilibrium crystallization sequence, where plagioclase begins to crystallize before pyroxene (Fig. 3). In all cases, early formed spinels are euhedral, nucleating on the Pt wire or the melt-gas interface. At the slower cooling rates, spinel nuclei are rare, resulting in large (up to 1 mm) spinel crystals. In some of the faster cooled experiments, a second generation of ragged spinels grew along with the melilites in the interior of the charge. The textures of the run products are dominated by dendritic melilites that result in a herringbone pattern texture (Fig. 4). Pyroxenes grow between the limbs of the melilite dendrites.



FIG. 4. 2°C/hr., field of view 1.4 x 2.1 mm

Textures resembling those produced in these experiments do not appear to have been observed in CAIs. In addition, anorthite crystallization appears to have preceded or been nearly simultaneous with pyroxene crystallization in coarse-grained CAIs (11). Although the cooling rates studied are slower than those expected for radiative cooling of molten droplets (12), the failure of these experiments to reproduce CAI crystallization sequences (i.e., plag before or simultaneous with pyroxene) or textures (in contrast to the success of experiments on chondrules [12]), suggests that coarse-grained CAIs were never totally molten, that the subcooled liquid model for their origin (4) does not apply, and that cooling rates were slower than 20°C/hour in order to account for the early appearance of plagioclase in the crystallization sequences. However, a larger range of experimental conditions will have to be explored before these suggestions can be confirmed.

References: (1) Clayton D.D. (1980) *Astrophys. J.* 239, L.37. (2) Armstrong J. et al. (1982) *G.C.A.* (in press). (3) Clayton R.N. et al. (1977) *EPSL* 34, 209. (4) Blander M. and Fuchs L. (1975) *G.C.A.* 39, 1605. (5) Dowty E. and Clark, J. (1973) *Am. Mineral* 58, 230. (6) Andersen D. and Lindsley D. (1981) *LPS XII*, 19. (7) Haggerty S. (1978) *Nature* 276, 221. (8) Mao H.K. and Bell P. (1974) *Geophys. Lab. Yrb.* 73, 488. (9) Grossman L. (1972) *G.C.A.* 36, 597. (10) Stolper E. (1981) *LPS XII*, 1049. (11) MacPherson G. and Grossman, L. (1981) *EPSL* 52, 16. (12) Tsuchiyama A. et al. (1980) *EPSL* 48, 155.

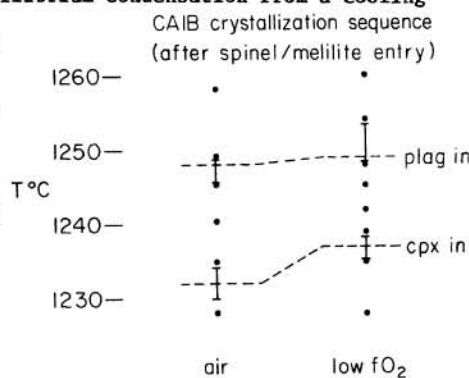


FIG. 3